SCIENTIFIC REPORTS

OPEN

SUBJECT AREAS:
MICRO-OPTICS
BIOMIMETICS
OPTOELECTRONIC DEVICES AND COMPONENTS

Received
13 May 2014

Accepted
19 August 2014

Published
5 September 2014

Correspondence and requests for materials should be addressed to J.K. (plasmon@iastate.edu)

Absorption-assisted mode transformation in butterfly compound eyes

Jaeyoun Kim

Department of Electrical and Computer Engineering, Iowa State University, Ames, Iowa, 50011, USA.

The ommatidium of the butterfly's afocal apposition eye exhibits angular performance that can only be achieved by transforming the diffraction pattern of its corneal lens into the fundamental mode of its rhabdom waveguide. A graded index model of the ommatidium has been proposed and verified but the efforts to extract the transformation's underlying physics from it have been hindered by its extreme complexity. Here we numerically investigate the ommatidium model and reveal that the current model, involving only the graded index distribution, is insufficient for the transformation. We further find that adding spatially varying absorption to the existing model dramatically improves its transformation performance, producing near-perfect mode matching with overlap integral exceeding 0.96. Such a combined action of spatially varying index and absorption for microscale mode transformation is new to researchers in optics and biology and will benefit both disciplines.

Insects' compound eyes achieve their wide field-of-view using hemispherically arrayed optics[1]. In the apposition type, one corneal lens (*CL*) and one rhabdom (*Rh*) form a lens-waveguide pair which, along with other parts between the two, is collectively called an ommatidium (Fig. 1a). For optical isolation between ommatidia, the level of light coupled into *Rh* depends critically on the incidence angle θ_i. The angular response typically peaks at normal incidence ($\theta_i = 0$) and tapers off as θ_i increases. The acceptance angle θ_A marks the full-width half-maximum point of the response curve[1–3]. In the superposition type, in contrast, each *CL* collects rays over a wide angular range. Then the crystalline cone (*CC*) collimates them for redistribution over multiple photoreceptors (Fig. 1b)[1,4].

Nilsson *et al.* found a third type in butterflies[5]. Structurally, it is an apposition eye comprising a large number of ommatidia. But it also resembles the superposition eye in collimating its output using the cone stalk (*CS*) as the collimation lens (Fig. 1c). These mixed characteristics positioned this third type, called *afocal* apposition eye for its perfect collimation, as the link between the apposition and superposition eyes[5,6].

At question was how an apposition eye came to employ collimation which does not give clear advantages while requiring very complex *CS* architectures. For instance, with its unique index distribution, *Heteronympha merope*'s *CS* produces 0.2 mega-diopters of magnification from just ~10 μm in length, making itself "*the most powerful known to man.*[5]"

Nilsson *et al.* provided a clue by revealing another role of *CS*[7]. As mentioned above, ommatidial isolation requires reductions in θ_A. Optically, θ_A minimizes when the electric field pattern hitting the *Rh* waveguide entrance exactly matches that of the waveguide's fundamental mode (LP_{01}). However, *CL* generates Airy-like patterns that are different from LP_{01}. In typical apposition eyes, the mismatch broadens θ_A by ~15% from its theoretical minimum[6,7]. In contrast, the afocal apposition eye's θ_A turns out to match the theoretical minimum, indicating that *CS* transforms the Airy-like pattern into LP_{01}. Collimation is just a part of the mode transformation process.

The search for the transformation mechanism has produced a graded index model of the ommatidium[8] and multiple hypotheses. One interpreted *CS* as a waveguide mode coupler[7]. Since Airy pattern closely resembles the sum of the two lowest axis-symmetric modes, LP_{01} and LP_{02}, *CL* practically excites both modes into *CS*. Totally transferring LP_{02}'s mode power towards LP_{01} will realize the LP_{01} transformation. Another suggested that *CS* functions as a mode mixer which synthesizes LP_{01} from the local modes of the tapered, index-graded *CS*[8]. So far, theoretical efforts to verify the hypotheses have been thwarted by the model's extreme complexity.

Here we analyze the LP_{01} transformation mechanism numerically. We find that the existing graded index model is insufficient for the task. Complementing it with spatially varying absorption, however, has directly led to successful LP_{01} transformations. Such a combined action of non-uniformly distributed index and absorption gives the afocal ommatidium a new interpretation as an absorption-assisted mode shaper, rather than a coupler or mixer. The new findings will enrich the knowledgebase of insect optics[1] and bio-inspired optics[9,10] alike.

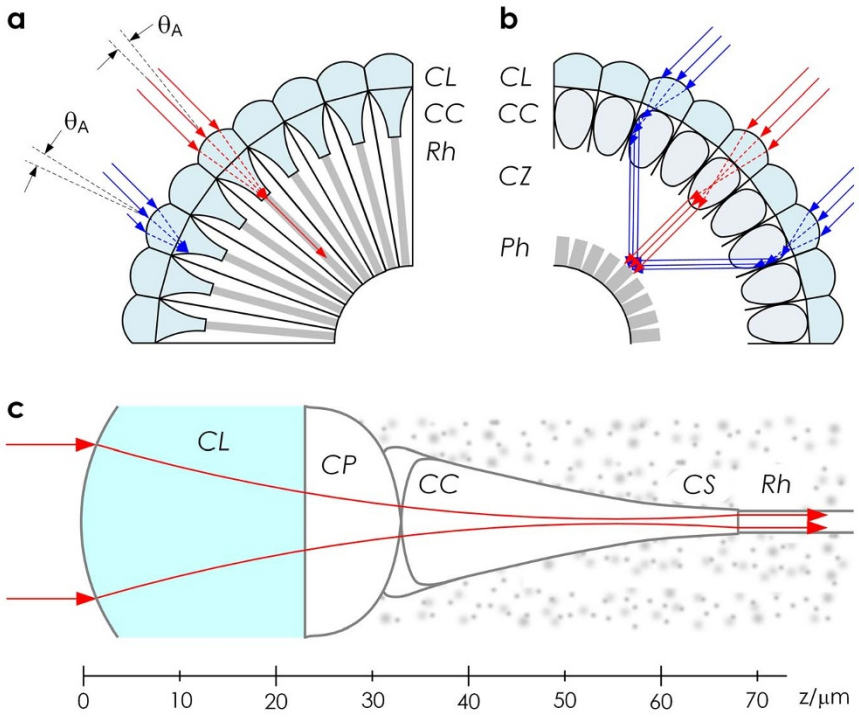

Figure 1 | Features of afocal apposition eye and its model. (a,b) Schematic diagrams of (a) apposition and (b) superposition compound eyes. The former consists of *CL-Rh* pairs. Each pair maximally accepts only the normally impinging ray with the level of acceptance tapering off as the incidence angle increases. The full-width half-maximum point of the curve marks the acceptance angle θ_A. In the latter, in contrast, *Ph* collects rays from multiple *CL*s. Light collimation by *CC* is essential for propagation across *CZ*. (c) The ommatidium of the afocal apposition eye. *CL* focuses light inside *CC*, not at the *Rh* entrance as in (a). Similar to the superposition eye, its *CS* collimates the defocusing rays. (*CL*: corneal lens, *CC*: crystalline cone, *CS*: cone stalk, *Rh*: rhabdom, *Ph*: photoreceptors, *CZ*: clear zone).

Results

Testing mode coupling/mixing hypotheses. With the numerical simulation code and ommatidium model set up as described in Methods, we first simulated the propagation of a plane wave through the afocal ommatidium to test the existing hypotheses. Figures 2a and b show that the simulation correctly reproduced the experimentally observed mid-*CC* focal spot formation ($z \sim 58$ μm). Despite the non-uniform index distribution in *CC*, the focal field pattern closely matched Airy pattern, both in amplitude and phase (Fig. 2c). Existing studies hypothesized that this Airy-like pattern would evolve into LP_{01} through mode coupling or mixing as it approaches the *Rh* entrance at $z = 68$ μm[7,8].

However, the amplitude and phase profiles obtained at that point, shown in Fig. 2d, exhibited high-level mismatches from those of LP_{01}. The side-lobes of the Airy-like pattern persisted throughout *CS*, leaving severe wiggles to the final amplitude profile. The step-like phase distribution in Fig. 2c has been quasi-linearized as shown in Fig. 2d but it is still insufficient to match the flat wavefront of LP_{01}. Only the width of the field pattern matched that of LP_{01} reasonably at the *Rh* entrance.

To quantify the level of mode matching, we introduced three metrics in Methods: the shape error δ_s, phase error δ_p, and the overlap integral η which considers both shape and phase. The inset in Fig. 2b shows the computed η as a function of z. Even within *CS*, η increases very slowly, only to reach 0.77 at its end. The values of δ_s and δ_p are also large, reaching 0.0603 and 0.6068 at the *Rh* entrance, respectively. Simulations performed at different wavelengths with slightly varied structural parameters, including the *CP* thickness, *CC* length, and *CS* index profile, all produced similar mismatch. It indicates that mechanisms relying solely on the graded index distribution of *CS*, such as mode coupling or mixing, are insufficient to transform the Airy-like pattern into LP_{01}.

Impact of distributed apodization. The intensity distribution in Fig. 2a shows that the wiggles in the final amplitude profile evolved mainly from the outermost fringe of the *CL*-focused light. So we attempted to suppress the wiggles by blocking the fringe with an annular absorptive region. It is analogous to the apodization process in Fourier optics which removes the peripheral, high spatial frequency portion of a diffraction pattern[11]. Removal of the wiggles alone, however, does not guarantee LP_{01} transformation. It hinges on whether the subsequent geometry and index distribution, already given by Nilsson *et al.*[5,6] and Pask *et al.*[8], can correctly modify the amplitude and phase of the apodized wave.

We explored its feasibility with iterative simulations. We assumed that the absorption is mild yet broadly distributed and implemented it by making the portion of *CC* with $\rho \geq a$ and $z \geq z_o$ weakly absorbing in our numerical model, as shown in Fig. 3a. We empirically set the electric field attenuation at 1% per 50 nm or 0.873 dB·μm^{-1}. Given the existence of light-absorbing pigments around the ommatidium, this type of distributed absorption in *CC* seems plausible[12,13]. Figure 3b shows the intensity distribution from an exemplary simulation. The absorptive region apparently blocked most of the outermost fringe.

The apodization impacted LP_{01} transformation immediately. Figure 3c shows the amplitude and phase profiles obtained at $z = 67.4$ μm, right in front of the *Rh* entrance, with $(z_o, a) = (33, 2.4)$ μm. Comparison of the amplitude profile with that of LP_{01} reveals that the apodization was very effective not only in removing the wiggles but also in reshaping the overall mode profile into that of the single-peaked LP_{01}. The computed shape error δ_s was 0.0216, a factor of 3 reduction from that of the unapodized one.

It is important to point out that the distributed absorption greatly improved the phase profile matching as well, even though it cannot directly affect phase. At the same z point (67.4 μm), the phase error

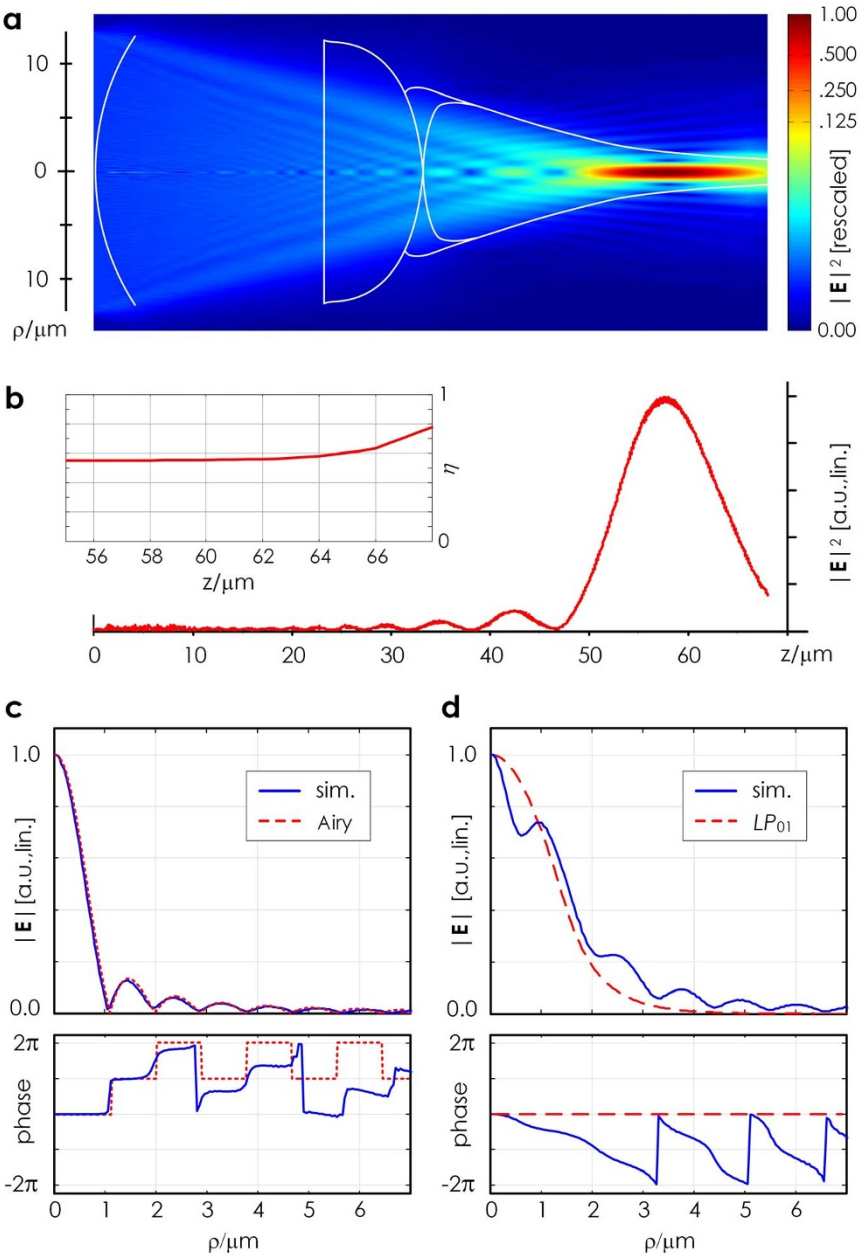

Figure 2 | Testing mode coupling/mixing hypotheses. (a) and (b) show the intensity distribution and the change in its center axis intensity resulting from the simulated propagation of a plane wave through the ommatidium model in Methods. Both confirms the mid-*CC* focusing by *CL* near $z = 58$ μm. The inset in (b) shows the change in the overlap integral η between $z = 55$ and 68 μm. (c) The amplitude and phase profiles at the focal spot ($z = 58$ μm). They agree well with those of Airy pattern except for the peripheral, low-intensity part ($\rho > 5$ μm). (d) The amplitude and phase profiles obtained at the *Rh* entrance ($z = 68$ μm), however, exhibit significant mismatches from the *Rh* waveguide's LP_{01} mode, indicating that the hypothesized mode coupling or mixing mechanism is insufficient for transforming an Airy-like pattern into LP_{01}.

δ_p was 0.0178, a factor of 34 improvement from the unapodized one. The inset of Fig. 3c visualizes the flatness of the wavefront across the radial extent of *CS* ($\rho \leq 1.3$ μm). We attribute this improvement again to the apodization which suppressed the peripheral portion with its phase quadratically retarded by *CL*.

The results of iterative simulations shown in Fig. 4 further reveal that such large δ_p improvements near the *Rh* entrance is possible only within a narrow window with $33 < z_o < 36$ μm and $2.1 < a < 2.5$ μm, reaffirming the need for a precise and complete elimination of the outermost fringe. A simultaneous reduction of δ_s within the window, however, was hindered by the persistent bulging near $\rho = 2$ μm (Fig. 3c). Since the level of shape matching within the radial extent of *CS* remains excellent, the bulging must be due to the absence of absorption outside the terminal portion of *CS*, which is evident in Fig. 3a.

Refinement by conformally extended absorption. So we extended the absorption region as shown in Fig. 5a. Starting from $z = z_t$, the exterior of *CS* was made absorptive all the way to the original apodization region. A thin buffer layer with thickness t was installed for fine control. For simplicity, we set the electric field attenuation within this conformally extended absorption region identical to that of the apodization region, *i.e.*, 0.873 dB·μm^{-1}. Then we performed iterative simulations involving all four parameters: z_o (33 ~ 36 μm), a (2.1 ~ 2.5 μm), z_t (65 ~ 67 μm), and t (0 ~ 0.5 μm) and again observed additional improvements in

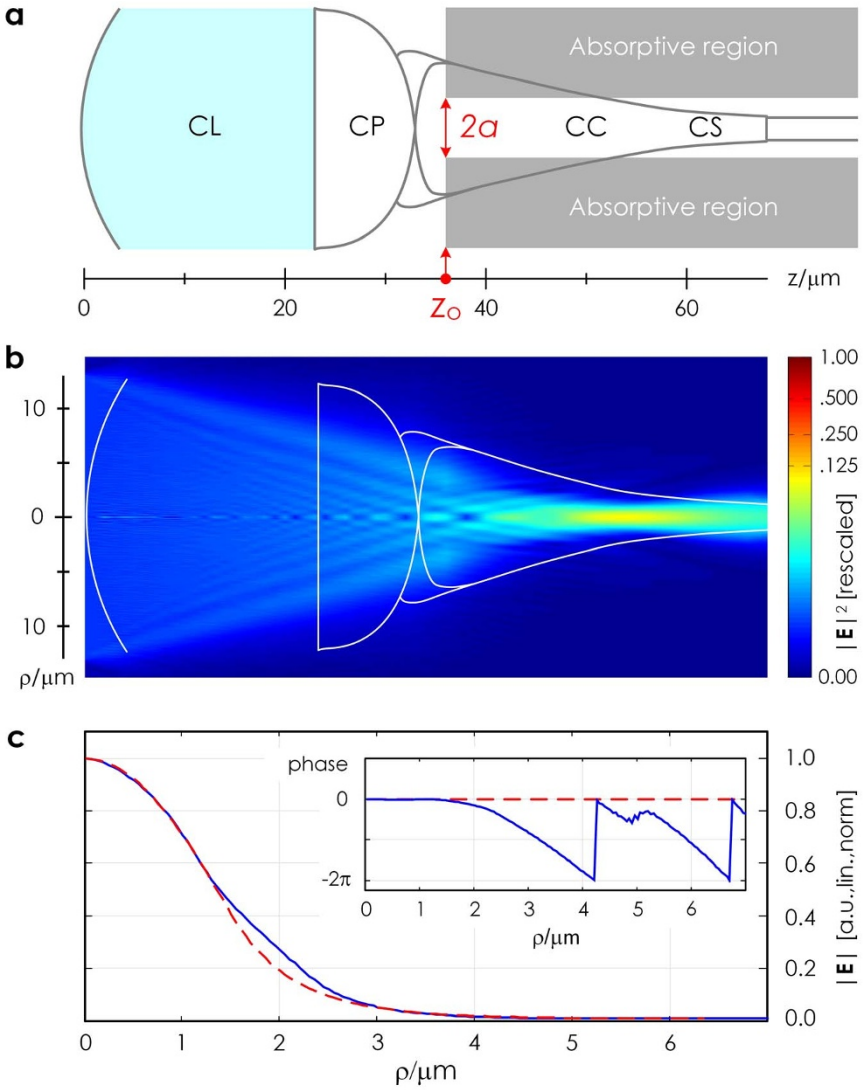

Figure 3 | Absorptive apodization and its impact. (a) The setting of the hypothesized absorptive apodization. Low-level absorption (0.873 dB μm^{-1}) was implemented in the region with $z > z_o$ and $\rho > a$. (b) Intensity distribution obtained from an apodized propagation simulation with $(z_o, a) = (36, 2.3)$ μm. Blocking of the outermost fringe is evident. (c) The amplitude and phase profiles obtained at z = 67.4 μm at which the phase error δ_p becomes minimized. The dotted red curves represent LP_{01} which also appeared in Fig. 2 d. The bulging in the amplitude profile for $\rho \sim 2$ μm persisted for other values of (z_o, a), necessitating additional mode shaping.

LP_{01} transformation. We present the results obtained with $(z_o, a) = (36, 2.4)$ μm as examples.

Figure 5b shows the amplitude profile obtained at $z = 67.9$ μm with the value of t fixed at 0.35 μm. When $z_t = 65$ μm, the bulging near $\rho = 2$ μm disappeared completely, enabling the amplitude profile to overlap that of LP_{01} almost perfectly. The corresponding $\delta_s = 0.0049$, a factor of 5.3 reduction from the Fig. 3c result. The absolute difference between the amplitude profiles of the simulation results and LP_{01}, plotted in the inset, shows that the match improves increasingly as the conformally extended absorption region becomes longer. Figure 5c shows the phase profile at the same z-point as a function of z_t. Just as the apodization did, this conformally extended absorption further reduced the phase error values by flattening the wavefront. When $z_t = 65$ μm, it became near-flat within the radial extent of *CS*. The simultaneous minimization of δ_p and δ_s enabled the overlap integral η to reach 0.9646 at the *Rh* entrance.

The minimum phase and shape error values ($\delta_{p,min}$ and $\delta_{s,min}$) plotted in Fig. 5d show that simultaneous δ_p - δ_s minimization is limited to a narrow window of (z_t, t) combinations. The values of the optimal (z_t, t) combinations were also different for different (z_o, a) combinations. So, we extracted from our iterative simulation data the combinations of (z_o, a, z_t, t) which minimize both δ_p and δ_s at $z > 67.5$ μm, *i.e.*, within 500 nm of the *Rh* entrance, while maintaining $\delta_s < 0.01$. Table 1 lists them along with their performance metrics. It shows that the optimal values for z_o fall within a 3 μm range from the *CC* starting point, with the majority at $z_o = 35$ μm. The optimal values for the apodization pupil radius a are unanimously at or near 2.5 μm, which is approximately 42% of the *CC* radius at its starting point. The optimal z_t and t values exhibit only weak variations within $1 \sim 3$ μm and $0.2 \sim 0.4$ μm range, respectively. As shown in Fig. S1 in Supplementary Information, these configurations are effective over a wide spectral range spanning 400 to 600 nm.

Since the proposed LP_{01} transformation relies on absorption, it inevitably reduces the mode power. For optimal configurations in Table 1, they can be $73 \sim 77\%$ of the initial value. As shown in Fig. 5e, the initial apodization claims ~5 dB and the extended absorption another ~1 dB. The overall loss of 6 dB may seem high in power budget point of view. Removing the collimating *CS* and the absorptive mode transformation altogether, however, results in a situation in

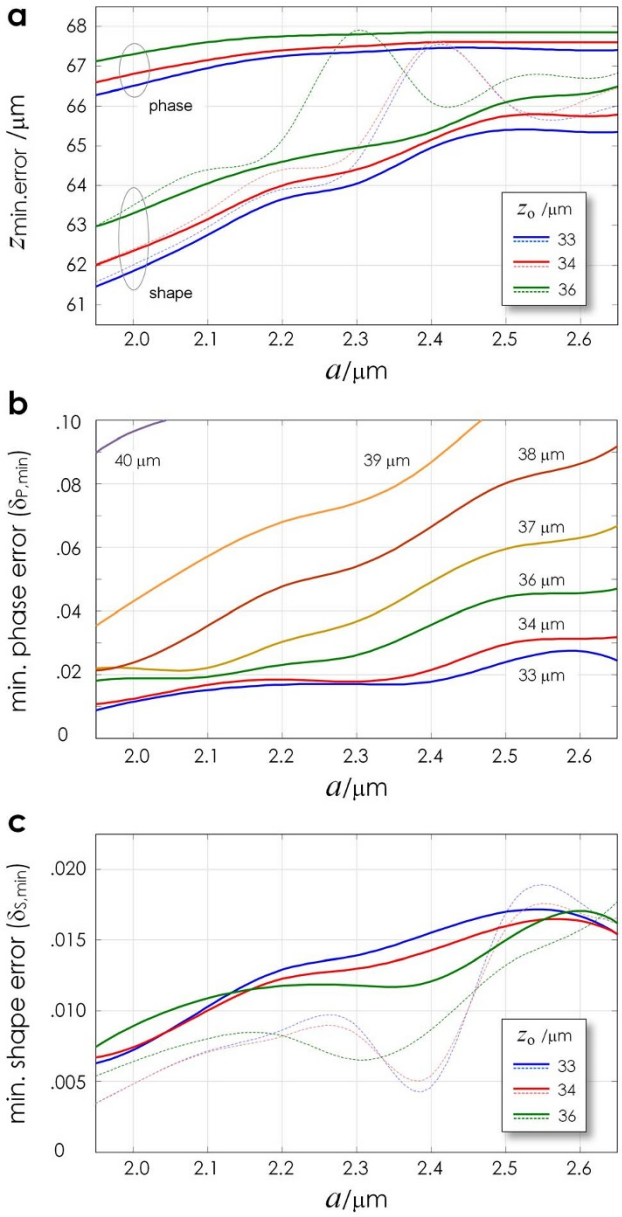

Figure 4 | Parametric search for simultaneous minimization of δ_s and δ_p. (a) Solid curves: *z*-positions at which the phase and shape errors minimize for the given (z_o, *a*). Lack of their intersection indicates that the two do not minimize simultaneously. Dashed curves: $z_{min,error}$ values obtained by limiting the range for the shape error evaluation within $\rho \leq 1.3$ μm, which enabled simultaneous minimization of δ_s and δ_p. (b) $\delta_{p,min}$ values as a function of (z_o, *a*). In general, δ_p grows rapidly as z_o moves away from *CP*. (c) Solid curves: $\delta_{s,min}$ values obtained when $z_o = 33 \sim 36$ μm, *i.e.*, within 3 μm from the ending point of *CP*. Overall, δ_s values grow monotonically with *a*. Dashed curves: δ_s assessed only within $\rho \leq 1.3$ μm. Now they exhibit definite dips, suggesting that the shape error accumulates mostly in the region with $\rho > 1.3$ μm, *i.e.*, the area not covered by the distributed absorption shown in Fig. 3a.

which the exact Airy pattern tries to excite LP_{01}. The corresponding coupling efficiency is[14]:

$$\eta_{couple} = \left(\frac{2}{x}\right)\cdot(1-e^{-x})^2 \qquad (1)$$

where $x = 7.34\cdot(r_o/r_A)^2$, r_A is the Airy spot radius defined as $0.61\cdot f_{CL}\cdot\lambda_o/(n_{CL}\cdot a_{CL})$ and r_o is the modal field spot size for Gaussian-approximated LP_{01} which is ~1.7 μm for the present *Rh*. The resulting η_{couple} is ~6.7 dB. Table 1 shows that the present model incurs slightly *lower* loss while adding the advantage of LP_{01} transformation and, hence, θ_A minimization. This justifies the use of absorption for mode transformation. The last column of Table 1 also indicates that initiating the apodization early, *i.e.*, near the *CP*/*CC* interface, can increase η slightly but also incurs significant penalty to the mode power.

Discussion

In conclusion, we utilized numerical simulations to test the existing hypotheses on how the afocal ommatidium transforms the *CL*-generated Airy-like pattern into LP_{01} and push its acceptance angle towards the theoretical minimum. Our initial results showed that the hypothesized mechanisms relying solely on graded index distribution, such as mode coupling or mixing, cannot accomplish the LP_{01} transformation. We then found that complementing the existing graded index model with spatially varying absorption can dramatically increase the level of mode matching. Interestingly, the added absorption improved not only the shape matching, which is under direct influence of loss, but also the wavefront flatness. This wavefront-flattening operation seems to develop into the collimation step of the superposition eye. Such a combined action of distributed index and absorption for microscale mode transformation is novel with no previous report. Iteratively, we identified a window in parameter space capable of realizing LP_{01} transformation with overlap integral exceeding 96%. The 6 dB power penalty arising from the use of absorption can easily be justifiable given that the purely refractive model also imposes a comparable level of loss due to the Airy-to-LP_{01} mode mismatch even though it cannot bring in the added advantage of θ_A minimization predicted for the absorption-assisted model.

It needs to be emphasized that the LP_{01} transformation in this work was achieved with minimal modifications made to the already verified model of the afocal ommatidium. In biological ommatidia, those modifications, *i.e.*, distributed absorption within and around *CC*, can be realized with light absorbing pigments infiltrating and surrounding the ommatidia, respectively. In soft biological structures, achieving and maintaining the μm-scale dimensional precision for optimal LP_{01} transformation seems challenging. Given the existence of pigments capable of migrating around the ommatidium for dark/light adaptations, we can envision a possible adaptive control scheme which adjusts the pigment distribution to maximize the mode matching.

These findings will interest both optical engineers and biologists. The former may get excited at the prospect of realizing highly miniaturized mode converters that are coupled with microscale focusing lenses and/or formed in-fiber. The recent trend in optical communication to exploit various modes supported by multiple mode fibers[21] indeed necessitates new paradigms in optical mode conversion[22,23] and the new absorption-assisted scheme will certainly contribute to the efforts. The possible involvement of absorption in the operation of insects' ommatidia would motivate the latter to examine additional roles of absorptive pigments. Numerically reproducing the angular response of the afocal apposition ommatidium using a fully 3-dimensional model will give the present work an ultimate validation. Here we emphasize that the optimal configurations found in this work are by no means ultimate or exhaustive. They can be further refined once the currently unknown refractive index and loss distributions around *CC* become available and the possibility of finding purely refractive models capable of performing the required transformation, as suggested in Ref. 23, should not be ruled out either.

Methods

Numerical simulation of wave propagation. To efficiently simulate the optical wave propagation in the ommatidium, we utilized the finite-difference beam propagation method (FD-BPM)[15]. Specifically, we chose a version of FD-BPM customized for scalar wave propagation in an axially symmetric cylindrical space[16–20] and

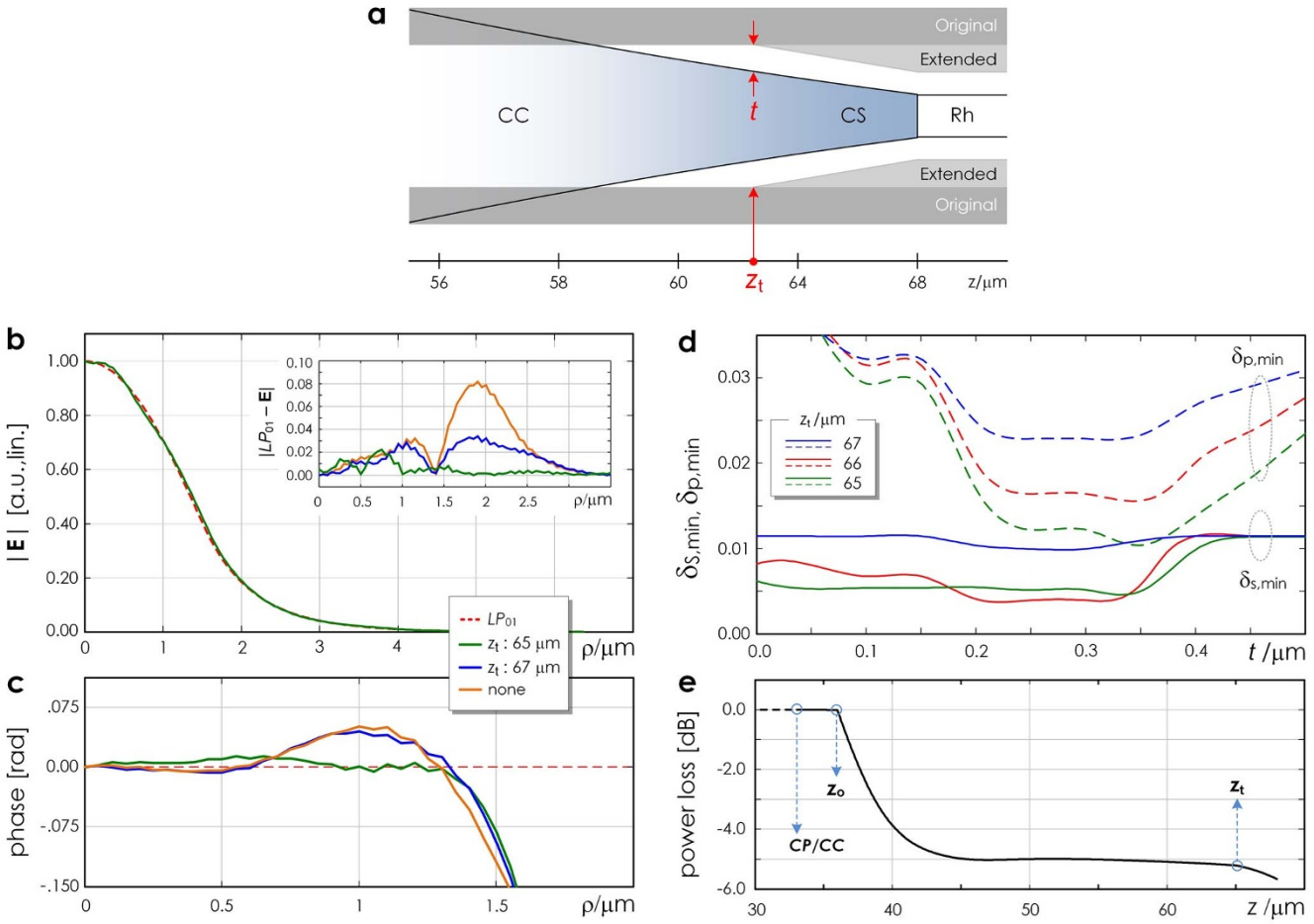

Figure 5 | Impact of conformally extended absorption. (a) The setting of the conformally extended absorption which starts from $z = z_t$ with a t μm-thick buffer. (b,c) The amplitude and phase profiles obtained at the *Rh* entrance when $t = 0.35$ μm. LP_{01} profiles are also superimposed for comparison. (b) For $z_t = 65$ μm, *i.e.*, 3 μm-long conformal absorption, the output becomes indistinguishable from LP_{01}. The inset shows how the increase in the conformal absorption reduces the mismatch in the output amplitude profile, especially near $\rho = 2$ μm. (c) The conformal absorption also improves the wavefront flatness within the radial extent of *CS*. (d) The minimum phase and shape errors for various (z_t, t) combinations. Note that δ_p and δ_s minimize simultaneously near (z_t, t) = (65 ~ 66, 0.2 ~ 0.35) μm. (e) The change in the mode power along the propagation through *CC* and *CS*. *CP*/*CC*: The interface between *CP* and *CC*.

implemented it with Matlab. Azimuthally changing modes, such as LP_{11} or LP_{21}, were inherently excluded. More universal methods exist for vectorial, azimuthally varying wave propagation but their computational burden was prohibitive for iteratively simulating a structure measuring over 15 μm in radius and 70 μm in length. Throughout our work, the radius of the simulation space was 20 μm. We used the transparent boundary condition to suppress spurious reflections from the edges of computation domain. The spatial resolution was fixed at 50 nm in both radial and axial directions. A full propagation typically took 15 ~ 30 seconds on computers with a *xeon* processor and 4 GB RAM. We validated the FD-BPM code by simulating the formation of Airy pattern by a spherical lens (Supplementary Figure S2). The wavelength λ_o was varied between 400 and 600 nm.

Table 1 | Configurations for LP_{01} transformation and results. (z_o, a, z_t, t) combinations producing simultaneous δ_p-δ_s minimization at $z > 67.5$ μm and $\delta_s < 0.01$. The corresponding δ_s and δ_p values can be found in the second column. The ratio between the final and initial mode power and the overlap integral η are given in the third column

z_o/μm	a/μm	z_t/μm	t/μm	δ_s	δ_p	P_f/P_i	η
33	2.5	3	0.4	0.008	0.012	0.237	0.973
34	2.4	1	0.2	0.009	0.015	0.229	0.973
34	2.4	2	0.3	0.008	0.013	0.229	0.972
35	2.4	2	0.2	0.003	0.015	0.247	0.968
35	2.4	2	0.3	0.004	0.012	0.248	0.969
35	2.4	3	0.2	0.006	0.014	0.245	0.968
35	2.4	3	0.3	0.005	0.010	0.244	0.970
36	2.4	3	0.3	0.005	0.012	0.272	0.963

***Heteronympha merope* ommatidium model.** Most structural and optical parameters in the ommatidium model were from Nilsson *et al.*[5,6] and Hateran *et al.*[7]: *CL* radius: $a_{CL} = 12.25$ μm, *CL* thickness: 23 μm, *CL* radius of curvature: 20 μm, $n_{CL} = 1.52$. $f_{CL} \sim 54$ μm. *CP* was modeled as a 10 μm-thick plate with $n_{CP} = 1.34$. The *Rh* parameters are also close to those of Nilsson *et al.*[5,6]: *Rh* diameter = 2.07 ~ 3 μm, $n_{Rh\_amb} = 1.35$, and $n_{Rh} = 1.36 \sim 1.38$. For the graded index profile and dimensions of *CC* and *CS*, we adopted the model proposed by Pask *et al.*[8]: $n_{CC}^2 = n_o^2 \cdot [1 + 2 \cdot \Delta \cdot (\theta_1^2 - \theta^2)/R^2]$ where $n_o = 1.4$, $\Delta = 131.5$, $\theta_1 = 0.1$ rad. R and θ were computed at each position within the *CC*. With the length of *CC* set to 35 μm[8], its radius decreases linearly from 6.1 to 1.3 μm as it approaches *Rh*. Pask *et al.* verified this model[8] by reproducing the experimental optical magnification data of Nilsson *et al.*[5] Supplementary Figure S3 shows the numerical model schematically.

Quantification of mode matching. To quantify how closely a simulated electric field distribution matches that of LP_{01}, we utilized three metrics. The shape error δ_s is defined as:

$$\delta_s = \sqrt{\iint \left(|E_{sim}|^2 - |E_{ref}|^2 \right)^2 ds} \Big/ \iint |E_{ref}|^2 ds \qquad (2)$$

where E_{sim} and E_{ref} represent the electric field distributions obtained from the simulation and the exact LP_{01} mode solution, respectively. Since our FD-BPM presumes total axis-symmetry, the cross-sectional integration was actually performed only along the radial direction. Two different integration ranges were used. For

overall shape error, the intensity distributions within $\rho = 0 \sim 7$ μm range was compared. When comparing only the center portion of the intensity distribution, the range was reduced to $\rho = 0 \sim 1.3$ μm. Since LP_{01} exhibit a flat phase distribution across its mode profile, we assessed the level of match in the phase with the phase error δ_p which is the standard deviation of the simulated phase response. Because *CS* manipulates only the center portion of the wave, δ_p was evaluated within the $\rho = 0 \sim 1.3$ μm range. To consider the impacts of both the shape and phase, we utilized the overlap integral η defined as

$$\eta^2 = \left| \iint E_{sim} \cdot E_{ref}^* \, ds \right|^2 \Big/ \left(\iint |E_{sim}|^2 ds \cdot \iint |E_{ref}|^2 ds \right) \quad (3)$$

Since η was used primarily for very similar field profiles, the integration range was fixed to $\rho = 0 \sim 7$ μm.

1. Land, M. F. & Nilsson, D.-E. *Animal Eyes* (Oxford University Press, New York, 2002).
2. Stavenga, D. Angular and spectral sensitivity of fly photoreceptors. I. Integrated facet lens and rhabdomere optics. *J. Comp. Physiol. A* **189**, 1–17 (2003).
3. Stavenga, D. G. Angular and spectral sensitivity of fly photoreceptors. II. Dependence on facet lens F-number and rhabdomere type in Drosophila. *J. Comp. Physiol. A* **189**, 189–202 (2003).
4. McIntyre, P. & Caveney, S. Graded-Index Optics are Matched to Optical Geometry in the Superposition Eyes of Scarab Beetles. *Phil. Trans. R. Soc. Lond. B* **311**, 237–269 (1985).
5. Nilsson, D.-E., Land, M. F. & Howard, J. Afocal apposition optics in butterfly eyes. *Nature* **312**, 561–563 (1984).
6. Nilsson, D.-E., Land, M. F. & Howard, J. Optics of the butterfly eye. *J. Comp. Physiol.* **162**, 341–366 (1988).
7. van Hateren, J. H. & Nilsson, D.-E. Butterfly optics exceed the theoretical limits of conventional apposition eyes. *Biol. Cybern.* **57**, 159–168 (1987).
8. Pask, C. & Bertilone, D. Evidence for a new optical element in insect visual systems. *J. Opt. Soc. Am. A* **6**, 139–141 (1989).
9. Lee, L. P. & Szema, R. Inspirations from biological optics for advanced photonic systems. *Science* **310**, 1148–50 (2005).
10. Kim, J., Jeong, K.-H. & Lee, L. P. Artificial ommatidia by self-aligned microlensesand waveguides. *Opt. Lett.* **30**, 5–7 (2005).
11. Goodman, J. *Introduction to Fourier Optics* (Roberts and Company Publishers, Greenwood Village, 2004).
12. Stavenga, D. G. Angular and spectral sensitivity of fly photoreceptors. III. Dependence on the pupil mechanism in the blowfly Calliphora. *J. Comp. Physiol. A* **190**, 115–129 (2004).
13. Stavenga, D. G. Reflections on colourful ommatidia of butterfly eyes. *J. Exp. Biol.* **205**, 1077–1085 (2002).
14. Pask, C. & Garth, S. J. Comparison of focal and afocal optics in insect eyes. *Biol. Cybern.* **58**, 337–344 (1988).
15. Okamoto, K. *Fundamentals of Optical Waveguides* (Academic Press, Orlando, 2000).
16. Yablon, A. D. *Optical Fiber Fusion Splicing*. (Springer-Verlag, Heidelberg, 2005).
17. Yamauchi, J., Nishio, K. & Nakano, H. Analysis of a lensed coreless fiber by a hybrid technique combining FD-BPM and FD-TDM. *J. Lightwave Technol.* **16**, 465–471 (1998).
18. Marcou, J., Auguste, J. L. & Blondy, J. M. Cylindrical 2D Beam Propagation Method for Optical Structures Maintaining a Revolution Symmetry. *Opt. Fiber Technol.* **5**, 105–118 (1999).
19. Shibayama, J., Takahashi, T., Yamauchi, J. & Nakano, H. Time-domain finite-difference BPM with Pade approximants in time axis for analysis of circularly symmetric fields. *Electron. Lett.* **36**, 319–321 (2000).
20. Hadley, G. R. Wide-angle beam propagation using Padé approximant operators. *Opt. Lett.* **17**, 1426–1428 (1992).
21. Bozinovic, N. *et al.* S. Terabit-Scale Orbital Angular Momentum Mode Division Multiplexing in Fibers. *Science* **340**, 1545–1548 (2013).
22. Heinrich, M. *et al.* Supersymmetry mode converters. *Nat. Commun.* **5**, 3698 doi: 10.1038/ncomms4698 (2014).
23. Markov, P., Valentine, J. G. & Weiss, S. M. Fiber-to-chip coupler designed using an optical transformation. *Opt. Express* **20**, 14705 (2012).

Acknowledgments

This work was supported by National Science Foundation through its grants ECCS-1147413 and ECCS-0954845.

Author contributions

J.K. conceived the idea, performed the analysis, and wrote the manuscript.

Additional information

Supplementary information accompanies this paper at http://www.nature.com/scientificreports

Competing financial interests: The authors declare no competing financial interests.

How to cite this article: Kim, J. Absorption-assisted mode transformation in butterfly compound eyes. *Sci. Rep.* **4**, 6291; DOI:10.1038/srep06291 (2014).